




Optimization of friction stir processing parameters for improving structural and mechanical properties in in situ AA5083-H111/Al–Fe composites

Proc IMechE Part C:
J Mechanical Engineering Science
1–14
© IMechE 2023
Article reuse guidelines:
sagepub.com/journals-permissions
DOI: 10.1177/09544062231211672
journals.sagepub.com/home/pic


Varun Singhal¹, Vivek Kumar Jain², Ravi Shankar Raman³,
Dinesh Patharia³, Vikas Mittal⁴, Subhash Mishra⁵ and
Hitesh Kumar⁶

Abstract

The primary focus of this study is the application of friction stir processing to produce surface composites of in situ AA5083-H111/Al–Fe. These composites were fabricated by mixing mechanically alloyed Fe–40 wt% Al powder for 40 h. The AA5083 substrate underwent a two-pass friction stir processing with changes in the tool's movement direction during fabrication. This experiment used Taguchi's L9 orthogonal array design to gather and analyse data efficiently. Following each friction stir processing pass, the fabricated aluminium metal matrix composite microstructure, hardness and ultimate tensile strength were conducted. In this study, the maximum tensile strength of 225.8 MPa after the first pass and 253.6 MPa after the second pass. Additionally, microhardness measurements indicated values of 123.3 and 128.3 Hv after the first and second passes, respectively. These impressive mechanical properties were achieved by optimizing specific process parameters, including a tool shoulder diameter of 21 mm, a tool rotational speed of 900 rpm, a tool traverse speed of 63 mm/min and a tilt angle of 1.5°. Furthermore, examining the fracture surface of the friction stir processed sample revealed ductile failure behaviour, suggesting that the material experienced deformation and stretching before fracture. This observation aligns with the inherent ductile nature of the AA5083/Al–Fe composite.

Keywords

AMCs, grain size, mechanical properties, L9 orthogonal array, fracture analysis

Date received: 19 July 2023; accepted: 16 October 2023

Introduction

Metal matrix composites (MMCs) are observed as advanced structural materials having a wide range of applications in aerospace, automotive, defence and marine engineering. These composites have several appealing features, including low weight density, high strength-to-weight ratios and improved corrosion resistance. MMCs are an attractive alternative for various structural applications due to their improved performance and efficiency in challenging settings.¹ Numerous conventional approaches are usually used to produce the MMCs, such as casting, powder metallurgy, mechanical alloying and plasma spraying.^{2–8} However, certain drawbacks to these procedures should be considered. One of the limits is the possibility of inadequate interfacial bonding between the metal matrix and the reinforced particles. This results in lower mechanical characteristics and degraded composite material performance.

Furthermore, the fabrication process might create significant stresses within the composite due to crystal structural mismatch between the matrix and reinforcement. This can have an impact on the composite

¹Department of Mechanical Engineering, GLA University, Mathura, Uttar Pradesh, India

²Department of Mechanical Engineering, Institute of Technology and Management, Maharajganj, Uttar Pradesh, India

³Department of Mechanical Engineering, ABES Engineering College, Ghaziabad, Uttar Pradesh, India

⁴Department of Electronics and Communication Engineering, Chandigarh University, Mohali, Punjab, India

⁵Department of Mechanical Engineering, IMS Engineering College, Ghaziabad, Uttar Pradesh, India

⁶Mechanical Engineering Department, TIET, Patiala, Punjab, India

Corresponding author:

Dr. Vivek Kumar Jain, Assistant Professor, Department of Mechanical Engineering, Institute of Technology and Management, Maharajganj, Uttar Pradesh 273303, India.
Email: vivekjain124@gmail.com

overall strength. Furthermore, surface contamination during manufacturing might affect the final composite properties and reliability. These drawbacks underline the importance of particular process optimization and quality control procedures to overcome these obstacles and ensure the composite desired performance.⁹

Furthermore, liquid route techniques may produce intermetallics at the interface between the matrix and the reinforcement.^{10,11} Indeed, a solid-state process that can provide strong interfacial strength between fine reinforcements and Al-alloy while maintaining homogenous reinforcement dispersion has to be developed.^{12,13} FSP in situ composites have shown the ability to achieve better interfacial bonding through in situ reactions. This results in superior mechanical characteristics because of the even distribution of smaller reinforcing particles created in situ. However, various other processing practices (sintering, casting, microwave synthesis and mechanical alloying are used to fabricate in situ aluminium composites.^{12–15} However, these process techniques require very expensive devices and consume excessive energy. In recent years, several investigations regarding FSP for in situ formation of MMCs were reported.^{14,16–18} In FSP, the reinforcement/matrix components react with each other, and intermetallic phases are formed by frictional heat and severe plastic deformation (SPD).^{18,19} FSP is an adaptation of FSW and the FSW was developed at TWI, UK, in 1991.¹¹ The FSP was started in 2003. FSP is based on friction stir welding (FSW), a solid-state joining procedure that allows materials to be joined without melting. However, rather than joining materials, FSP concentrates on changing their surface properties.²⁰ In FSP, a rotating cylindrical shouldered non-consumable tool comprising a profiled probe or pin is plunged into the work specimen surface and transferred along the processing direction (Figure 1). During friction stir processing (FSP), heat is generated through the rotating motion of the tool shoulder against the metal matrix. This heat causes the material to soften, and the material undergoes SPD due to the high strain rate.

In this direction, Al5083 plays a significant role in numerous engineering applications. Al5083 may not be heat treated and it is commonly used in marine, transportation and structural applications. The Al5083 alloy popularity can be attributed to its advantageous properties, which encompass lower density, a superior strength-to-weight ratio, outstanding weldability, remarkable corrosion resistance, favourable formability and moderate to high strength. Strength enhancement in the alloy is achieved through various mechanisms, including work hardening, dispersion strengthening and grain boundary strengthening. It is worth noting that work hardening, while contributing to increased strength, has a counterproductive impact on ductility and diminishes the material's toughness.^{21,22} In earlier studies, many researchers applied FSP to manufacture in situ Al–Al₃Ti,^{17,23} Al–Al₂Cu,²⁴

Al–Al₃Ni,^{14,25,26} Al–Al₁₂Mo,²⁷ Al₃Fe,²⁸ Al–Al₁₃Cr₂²⁹ and Al–Al₁₂Mg₁₇³⁰ composites. However, few works have been reported till now on the production of FeAl in situ AMCs using FSP.³¹ Iron–aluminium alloys are becoming more popular in high temperatures because stable second-phase particles are dispersed throughout the Al-alloy, even at elevated temperatures. As a result, these Al-alloys hold great potential as materials for a wide range of high-temperature situations. Lee et al.²⁸ produced an Al–Fe composite by multi-pass FSP on an Al–%10Fe billet made by powder metallurgy route. Moreover, increased FSP passes increase the Al–Fe reaction and formed the more intermetallic phases like Al₁₃Fe₄ in the composites. So that fabricated composite has enhanced the elastic modulus, tensile strength and hardness. Sarkari Khorrami et al.³² incorporated Fe particles in the matrix material by FSP and stated that the fabricated AMCs tensile strength was improved with finer grain structure after an increase in FSP passes. Azimi-Roeeen et al.¹⁶ fabricated in situ Al/(Al₁₃Fe₄ + Al₂O₃) hybrid composite from Al1050/Fe₂O₃ by FSP route and reported that the fabricated composites had improved hardness (45 Hv) and UTS (~171 MPa) value than the BM after four FSP pass. Azizieh et al.³³ synthesized in situ Al–Al₁₃Fe₄ surface composites via multi-pass FSP by the addition of Fe₂O₃ particles with AA1100 plate and reported that remarkable improvement in hardness (~300%) was achieved in the surface composites. In an investigation by Balakrishnan et al.,¹³ produced Al–Al₃Fe metal matrix composites (AMCs) by reacting molten aluminium and iron powder in situ. After the production, they used FSP to increase the mechanical and microstructural characteristics of the AMCs. Dinaharan and Murugan³⁴ conducted a study examining the impact of tool rotational speed, welding speed and axial force on the tensile strength of AA6061/10 wt% ZrB₂ composite joints. The highest tensile strength was achieved with a tool rotational speed of 1155 rpm, welding speed of 48.8 mm/min and axial force of 5.9 kN. Defects were observed in joints produced with parameter values either exceeding or falling short of these points. These findings were subsequently corroborated by several other researchers.^{35,36} Beyond tool rotational speed, welding speed and axial force, the geometry of the FSW tool is another crucial process parameter that affects material flow and joint properties.³⁷

The majority of published research work reported that for in situ surface composites, increased FSP passes played a vital role in the improvement in the particle distribution, microstructure, volume fraction of second-phase particles and mechanical properties of the SCs.¹⁸ In the current investigation, FSP is performed to fabricate the in situ AA5083/Al–Fe SCs and investigates the impact of process parameters on the microstructure, particle distribution and mechanical properties of the stir zone (SZ) in in situ Fe–Al AMC.

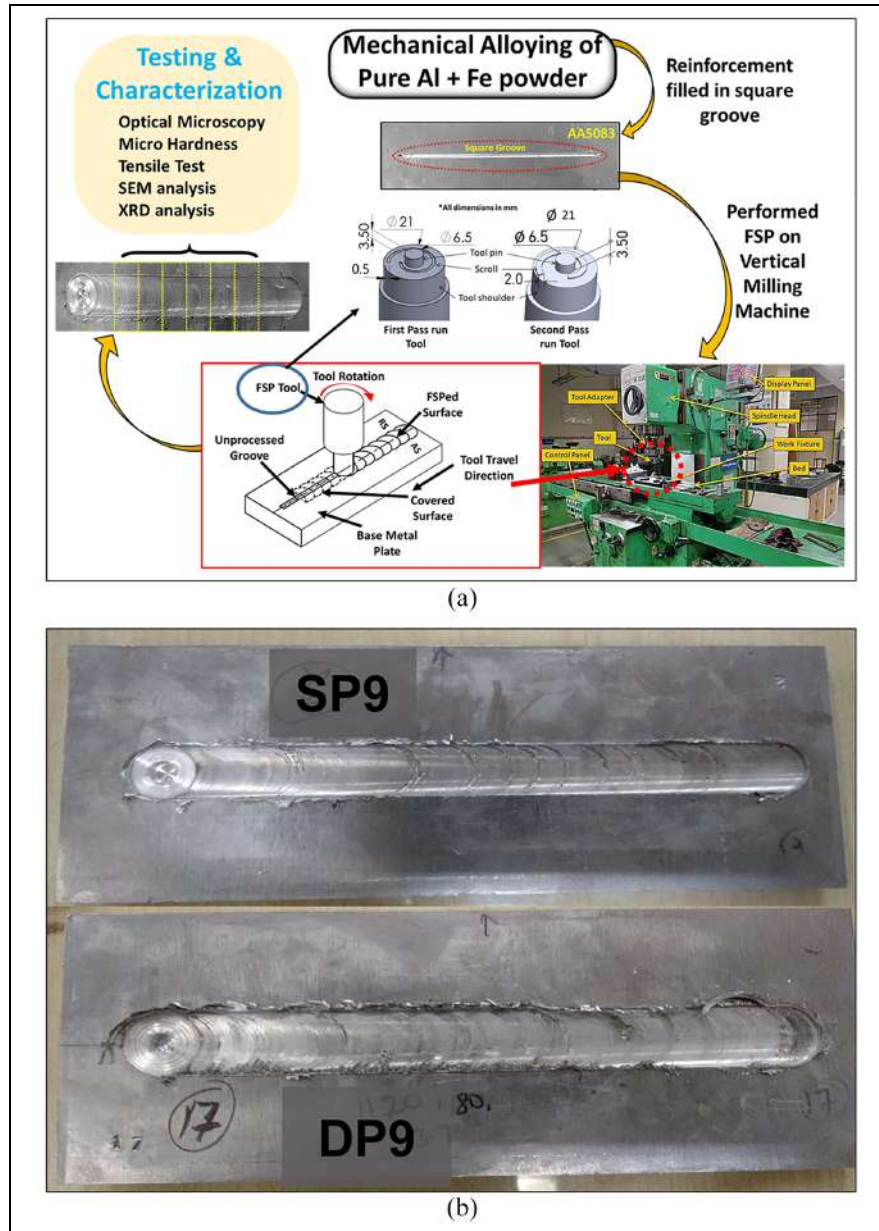


Figure 1. (a) Schematic diagram illustrating the friction stir processing and testing and characterization process and (b) represent the FSP processed Al-Fe reinforced AA5083 alloy specimen.

Experimental

Materials and methods

AA 5083-H111 alloy sheet of $20 \times 8 \times 0.63 \text{ cm}^3$ was used as a base alloy (BM). Table 1 displays the chemical concentration of the base material (BM). Figure 1 shows a 2.5 mm^2 square groove produced in the centre of each sample along the length direction. Figure 2(a) to (c) displays the SEM examination of Al-alloy powder, Fe powder and Al-Fe powder mixture. A powder mixture (Fe-40 wt% Al) was found from 40 h of mechanical alloying (MA) with an average particle size of $\sim 10 \mu\text{m}$. Within the processed regions of SCs, the actual reinforcement fractional volume levels (27.47 vol%). The theoretical

calculation of the fractional volume percentage was carried out using the equations (1–3).³⁸

$$\begin{aligned} \text{Tool pin area} \\ = \text{Diameter of tool pin} \times \text{tool pin length} \end{aligned} \quad (1)$$

$$\text{Goove area} = \text{Width of groove} \times \text{depth of groove} \quad (2)$$

$$\text{Frictional vol \%} = \left(\frac{\text{Goove area}}{\text{Tool pin area}} \right) \times 100 \quad (3)$$

However, the stir zone (SZ) area turned out to be larger than the projected tool pin area due to

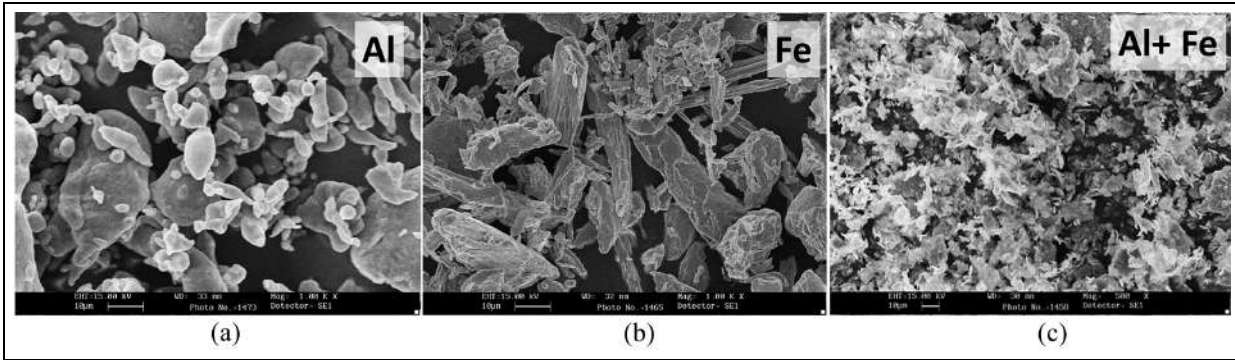


Figure 2. SEM micrographs of (a) Al-alloy, (b) Fe powder and (c) mixture of Al–Fe powder milled for 40 h.

Table 1. Chemical concentration of BM.

Constituent	Mg	Mn	Fe	Cr	Si	Ti	Zn	Cu	Al
BM (wt%)	4.81	0.54	0.212	0.097	0.044	0.014	0.010	0.008	94.265

extensive plastic deformation, resulting in a lower volume fraction of reinforcement than the theoretical vol%. When accounting for the SZ area, the actual vol% of reinforcement determined by equation (4).

$$\text{Frictional vol \%} = \left(\frac{\text{Goove area}}{\text{Area of SC}} \right) \times 100 \quad (4)$$

The Fe–40 wt% Al powder mixture was filled into the square slot during the fabrication process to create the appropriate shape. The top surface of the groove was initially packed using a 14 mm shoulder diameter pin-less tool.

In the friction stir processing (FSP) procedure, an H-13 steel tool was utilized with an RRVMC. The specific FSP parameters employed in this experiment consisted of a 6.5 mm pin diameter, 3.5 mm pin height and a 1.5° tool tilt angle. During single-pass FSP, a 21 mm tool shoulder diameter with an anti-clockwise (ACW) spiral scroll pattern was used, featuring a 0.75 mm scroll width and 0.5 mm scroll depth. For the second pass (double pass), a 21 mm tool shoulder diameter with an anti-clockwise (ACW) spiral scroll pattern was also applied. In this pass, shoulder profiles exhibited a 0.5 mm scroll height and 2 mm scroll width, as depicted in Figure 1. The extruded scroll was utilized to ensure a homogeneous distribution of reinforcement particles within the aluminium matrix.³⁹ Subsequently, a second pass was conducted using the second tool under the obtained optimum conditions on all the samples that had undergone the first pass of FSP. Adjustments to the tool scroll profile were made to address issues related to powder agglomeration. The study primarily focused on three crucial parameters: tool shoulder diameter (TSD), rotational speed (TRS) and traverse speed (TTS),

Table 2. For single-pass FSP, the range of chosen parameters is as follows.

Symbol	Parameters	Level		
		1	2	3
P1	TSD (mm)	16	18.5	21
P2	TRS (rpm)	710	900	1120
P3	TTS (mm/min)	63	80	100

with their respective values listed in Table 2–3. To determine the optimal process parameters for the investigation, rigorous testing was carried out on AA5083. A Taguchi design L9 orthogonal array was employed to optimize the parameter settings, resulting in a total of nine trials, as defined in Table 4. This approach allowed for a systematic exploration and evaluation of different combinations of parameters influenced the desired outcomes.

Moreover, specimens were obtained by employing wire electrical discharge machining (EDM) to cut from the processed area perpendicular to the welding path after each pass of FSP. For mechanical and microstructural evaluation, these specimens underwent thorough preparation. A high-quality surface finish was achieved on the samples using the usual metallographic method, ensuring reliable analysis and evaluation. Modified Poulten's reagent (2.5 mL HF, 30 mL HCL, 40 mL HNO₃, 12 g CrO₃ and 42.5 mL distilled water) was used as an etchant for 10 s. The macroscopic and microstructural examination was performed with a Stereo zoom microscope (Focus, Japan), OM (QS Metrology, India) and SEM (JEOL JSM 6610), respectively. Microhardness measurements of the samples were conducted at a distance of 0.1 cm below the topmost sample layer, with a

Table 3. Selected parameter for second pass FSP.

Symbol	Parameters	Level		
		1	2	3
P1	TSD (mm)	—	—	21
P2	TRS (rpm)	—	900	—
P3	TTS (mm/min)	63	—	—

Table 4. The experimental design used an L9 orthogonal array.

Exp. No.	P1	P2	P3	Sample ID	
				Single-pass FSP	Double pass FSP
1	1	1	1	SP1	DP1
2	2	2	2	SP2	DP2
3	3	3	3	SP3	DP3
4	1	2	3	SP4	DP4
5	2	3	1	SP5	DP5
6	3	1	2	SP6	DP6
7	1	3	2	SP7	DP7
8	2	1	3	SP8	DP8
9	3	2	1	SP9	DP9

horizontal spacing of 0.05 cm. A Vickers microhardness tester was employed for this measurement, applying a load of 10 N for a dwell period of 25 s. Tensile test coupons were removed from the processed zone (PZ) in the transverse direction per ASTM-EM08. Then, the fabricated specimens were sliced to 0.35 cm thickness with a CNC milling machine, and a test was done with a computer-interfaced tensometer.

Results and discussion

An extensive investigation was carried out to examine the reaction of FSP process factors on the manufactured surface composites (SCs). This analysis included microhardness, tensile testing, macrostructural evaluation and microstructural analysis.

Microstructure

Figures 3 to 8 shows processed macro and micrographs of SC made using FSP with single and double passes and various process parameters. These pictures show that Fe–Al dispersion is distributed within the Stir Zone (SZ) of the SCs. In most experiments (with single-pass FSP), the Fe–Al-reinforced powder particles were not dispersed efficiently in the metal matrix. They made clusters or aggregations in the SCs, as depicted in Figures 3(b) and 4(b). However, agglomeration sizes of reinforced particles in the samples are reduced considerably after performing another pass by a change in tool travel direction (CTTD), as shown

in Figures 7(b) and 8(b). It has been reported previously that CTTD between passes is an important method to improve powder particle distribution.^{40,41} CTTD between passes reverses the material flow confirmation from RS to AS and vice-versa. Reversed flow come across by CTTD results in more softening of the metal matrix and helps in improvement in the reinforcement particle distribution in the SZ.^{42,43} Due to reversed flow, Fe–Al powder particle distribution was enhanced after the second FSP pass, as evident in Figures 8 to 10.

Samples DP5 and DP9 were processed at the lowest TTS of 63 mm/min, and employing CTTD between passes exhibited better Fe–Al reinforced powder distribution in SZ (Figures 7 and 8). Improved Fe–Al reinforced particle distribution was detected on the AS through clearly distinct boundaries and bonding between the SZ of AS and BM as compared to RS because of different plastic deformation behaviour between the AS and RS.^{44,45}

It was discovered that the Fe–40 wt% Al particles were evenly spread throughout the material RS. The creation of equiaxed grains resulted from notable grain refining in the SZ. Refinement in the microstructure of Al-matrix with refined grains and larger zone of grain boundaries was obtained after the first pass of FSP. Incorporating Fe–Al particles reduced grain size from the initial size of 60 to 8–10 μm in a single pass of FSP. Figure 6(b)⁵ depicts that CTTD among passes reduced the grain size from 5.56–10 to 4.78–7.12 μm after the second pass in SZ due to dynamic recrystallization (DRX) during FSP.

Micrographs of SCs (Figure 4) fabricated at TTS of 1120 rpm, TSD of 18.5 mm and TTS of 63 mm/min with single-pass FSP exhibit meager material flow in the PZ. The size of accumulation in the AS is significantly large, with poor bonding with the metal matrix and tunnel defect resulting in a substantial drop in the strength of the SCs. Similar results are observed in the sample processed at TRS of 1120 rpm, TSD of 21 mm and TTS of 100 mm/min with single-pass FSP. However, when the sample was processed at TRS of 900 rpm, TRD of 21 mm and TTS of 63 mm/min with single-pass FSP, no tunnel defect was detected in the sample and reinforced particles were significantly distributed in the entire SZ as compared with the other samples.

In this order, the particles embedded in the matrix on AS may lead to non-homogeneous particle distribution. Homogeneous Fe–Al/matrix distribution was seen neighbouring the top surface compared to the underneath of SZ in all the processed SCs, owing to a higher temperature at the tool shoulder/metal boundary, which persuades additional softening. The top surface of the composites had a homogenous dispersion of particles, indicating that the particles were distributed evenly throughout the material. In Figure 9, an area mapping is presented to distribution of particles in the weld sample DP9. It is evident from Figure

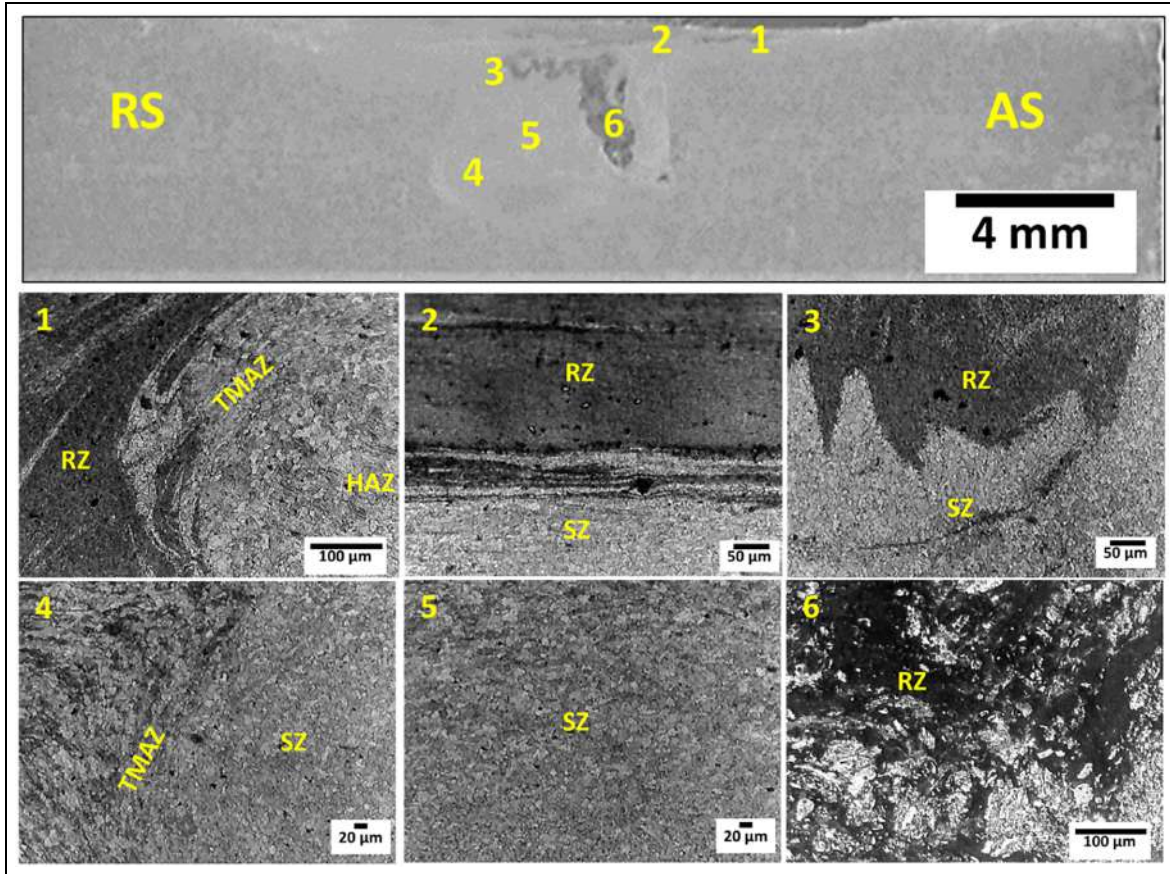


Figure 3. Macroscopic image of sample SP3 and several locations of the welding zone.

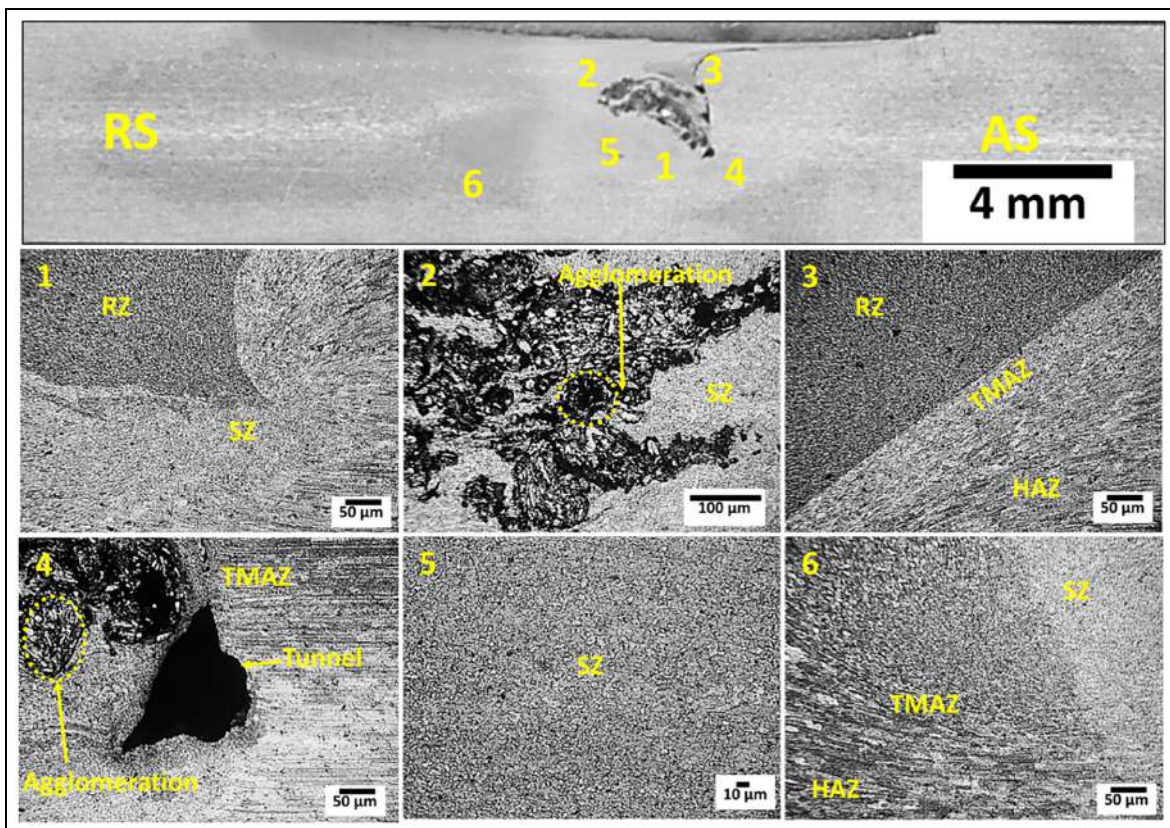


Figure 4. Macroscopic image of sample SP5 and several locations of the welding zone.

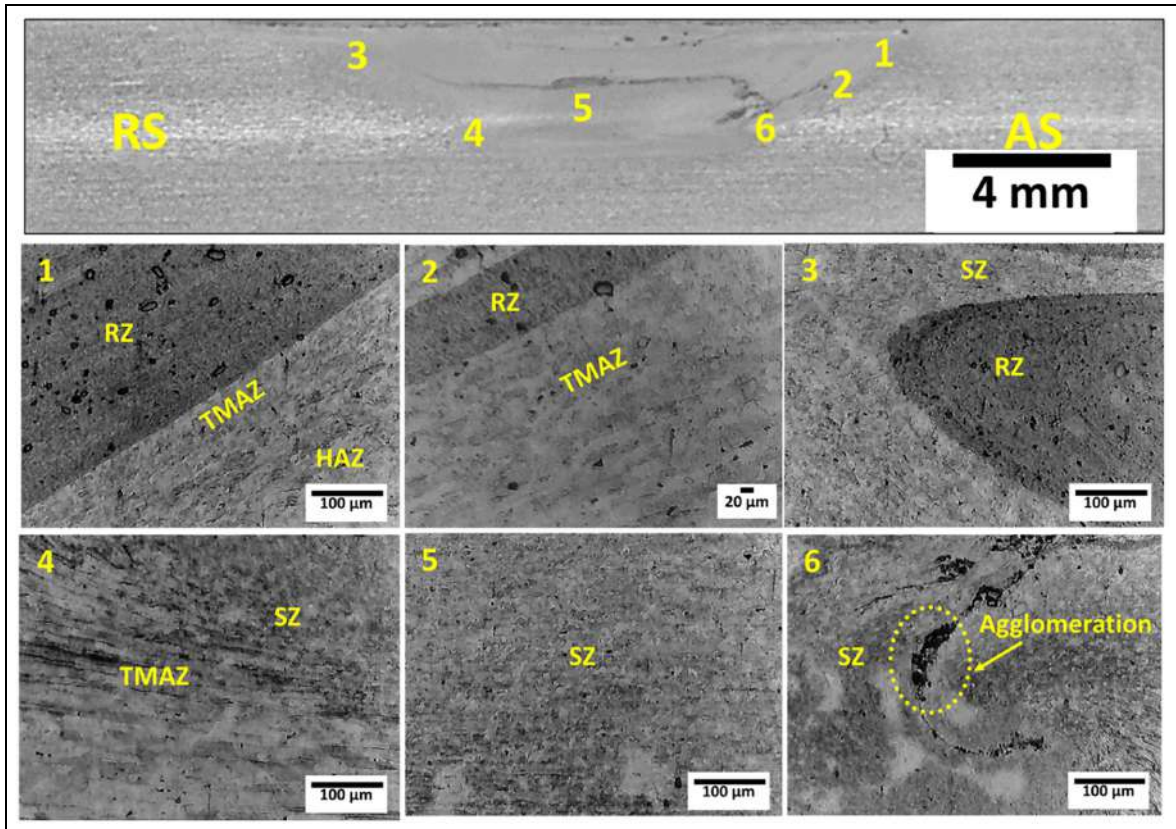


Figure 5. Macroscopic image of sample SP9 and several locations of the welding zone.

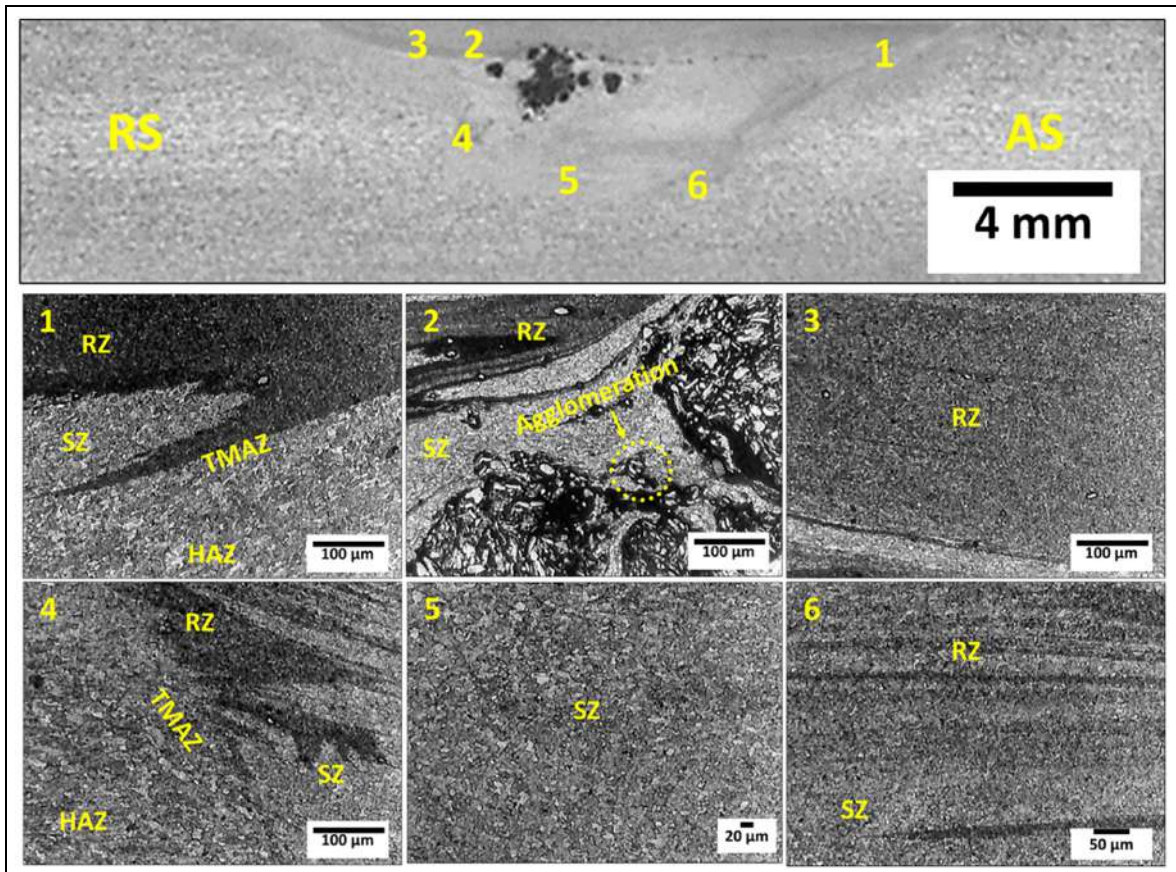


Figure 6. Macroscopic image of sample DP3 and several locations of the welding zone.

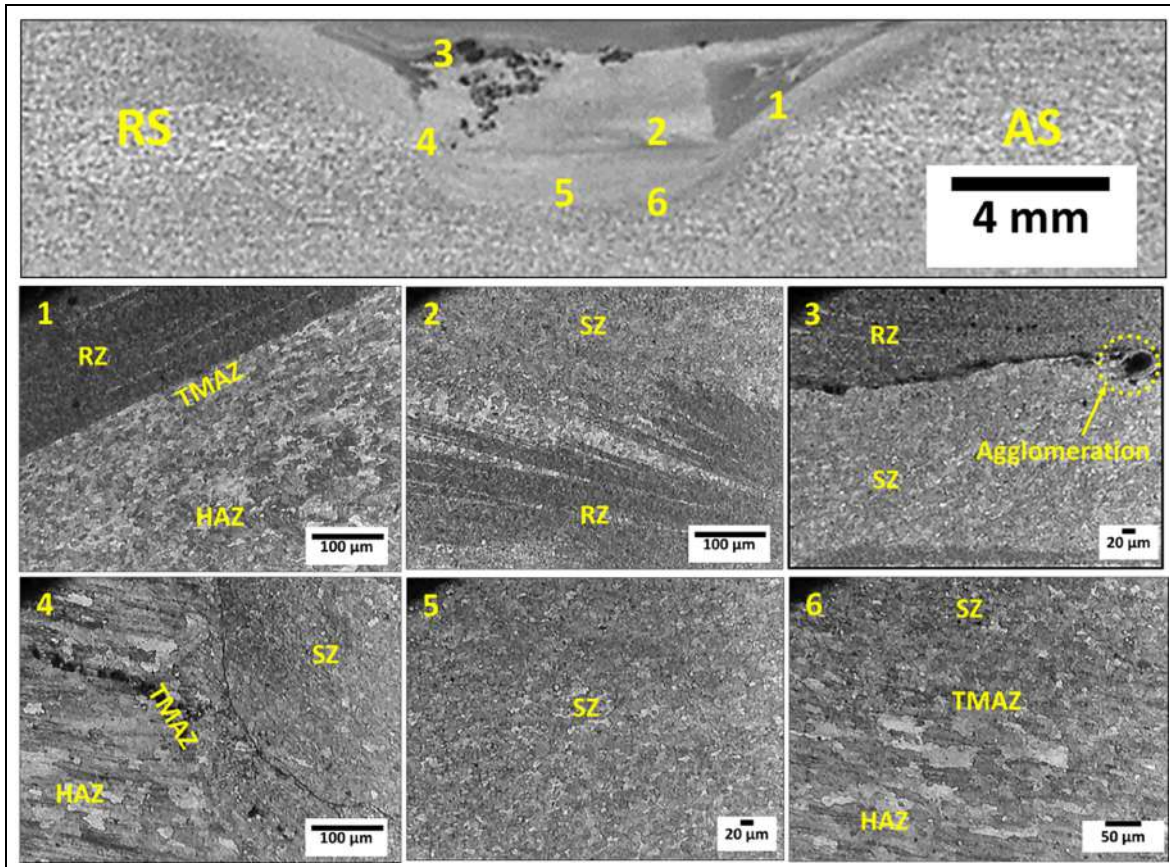


Figure 7. Macroscopic image of sample DP5 and several locations of welding zone.

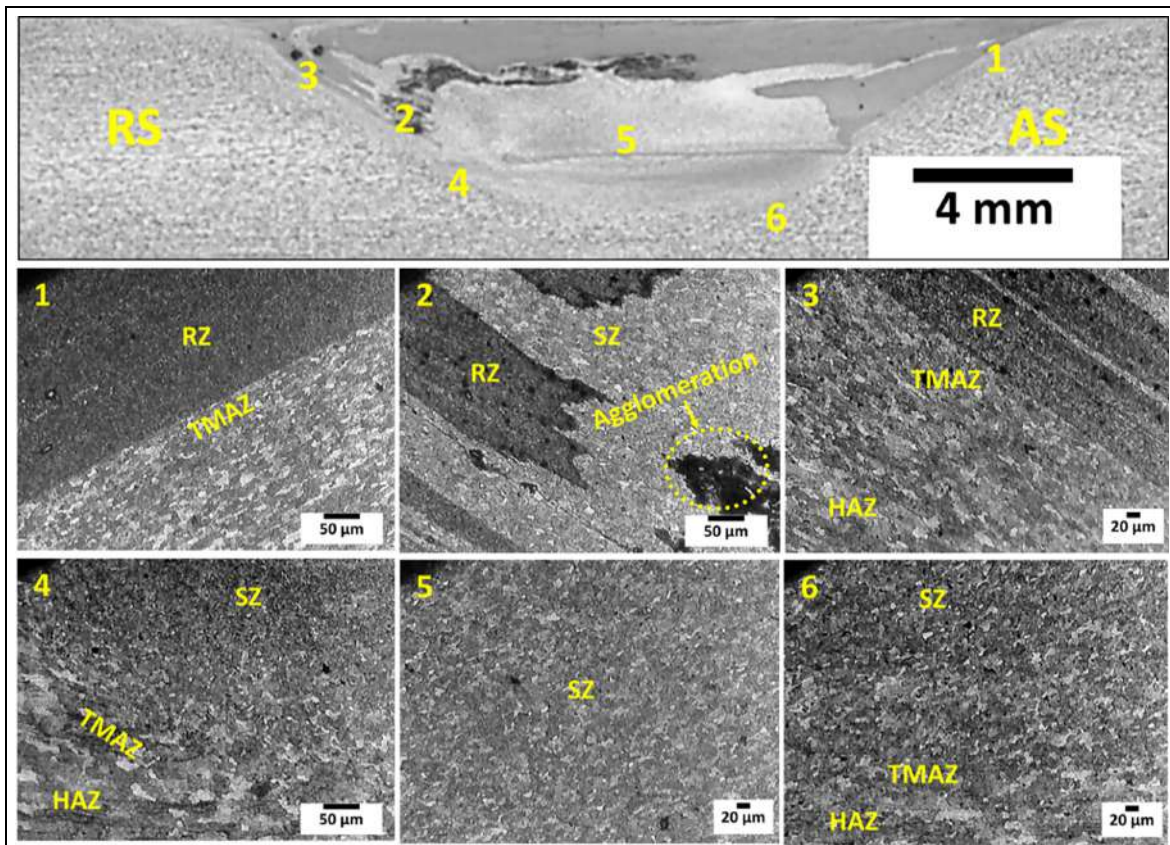


Figure 8. Macroscopic image of sample DP9, and several locations of welding zone.

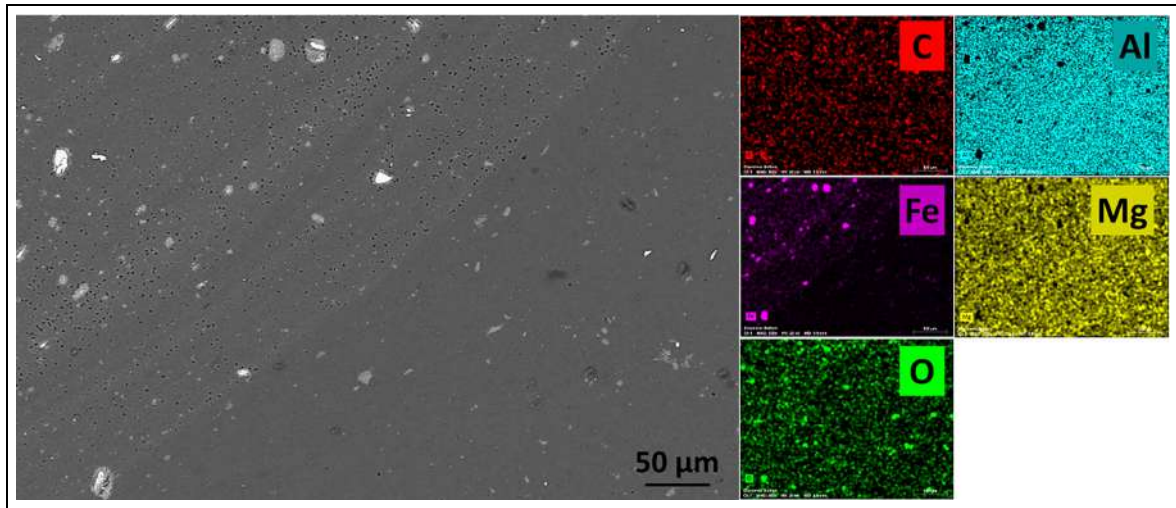


Figure 9. Area profile analysis of DP9 FSP sample.

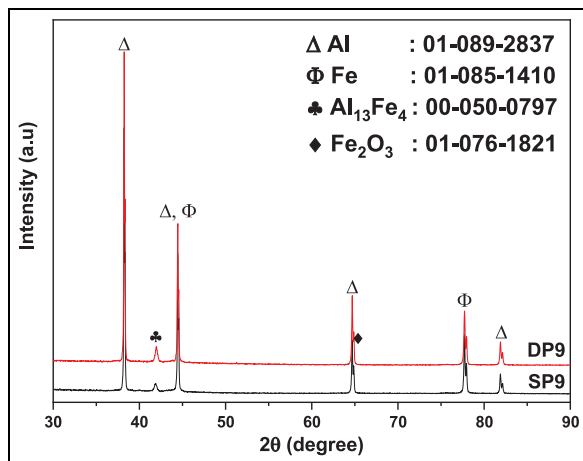


Figure 10. XRD analysis of SP9 and DP9 FSP sample.

9 that no defects are detected in the stir zone. The area profile reveals the existence of elements such as Al, Fe, Mg and O. Specifically, the weld zone of the DP9 sample exhibits a notable concentration of Fe elements. Moreover, the weld zone shows a high concentration of O, indicating the formation of intermetallic compounds like $\text{Al}_{13}\text{Fe}_4$ and Fe_2O_3 during the process of Friction Stir.

XRD analysis

A nugget was subjected to X-ray diffraction analysis on the stir zone of single-pass (SP9) and dual-pass (DP9) samples. The obtained diffraction data is displayed in Figure 10. The diffraction points observed sharp peaks of aluminium (Al) and iron (Fe) constituent phases in the nugget.

According to the investigation, intermetallic compounds such as $\text{Al}_{13}\text{Fe}_4$ and Fe_2O_3 have also been found in addition to aluminium (Al) and iron (Fe). These intermetallic compounds are produced in a very

short period of time during the FSP process due to the combined actions of heat and mechanical force.⁴⁶ The results of this investigation suggest that increasing the number of stirring passes in friction stir processing (FSP) improves the interaction between the Fe particles and the Al matrix. This accelerated reaction supports the development of the more intense phases. The Fe particles and Al matrix interact during FSP due to the rotating tool extreme plastic deformation and localized heating. The contact area between the Fe particles and the Al matrix expands with each consecutive stirring pass, enabling more significant interfacial mixing and reaction.

Hardness

The microhardness profile was produced by measuring the microhardness values at 1 mm beneath the top surface of the SC. These locations were uniformly spaced at intervals of 0.5 mm steps from the AS to the RS. Figure 11(a) displays the microhardness profiles of the single-pass FSP materials processed with different tool parameters. As seen from the microhardness curves, the microhardness plots in the SZ showed zig-zag trends in most of the samples due to improper mixing and powder agglomeration. Microstructural variation was observed in the different places of the SZ due to unlike material flow in the SZ, which causes variations in the strain, strain rate and temperature in the SZ.

The microhardness of SZ and TMAZ of SCs are higher than the BM hardness (81.9 Hv). There was significant variation in the hardness value at different tool shoulder diameters. Maximum and minimum average microhardness values of 123.3 and 94 Hv are obtained with tool shoulder diameters of 21 and 16 mm for samples SP₉ and SP₄ after a single pass FSP.

Figure 11(b) shows that the hardness curve for the samples processed with CTTD during the second pass

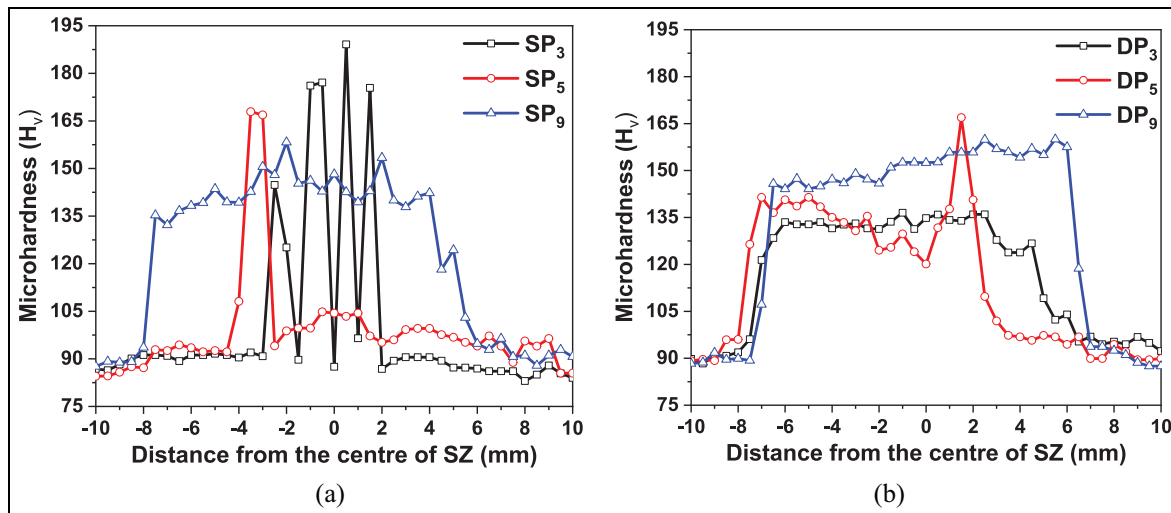


Figure 11. Microhardness plot of (a) single-pass SCs and (b) double-pass SCs.

exhibits better redistribution, improved dispersion and homogenization of the reinforcement particles compared to single-pass FSP.³³ The decrease in the variation takes place owing to the more uniform distribution of Fe–Al reinforced particles due to decreased grain size in the metal matrix, which improves particle density and increases restriction in metal matrix deformation during indentation, which enhances the hardness values. The hardness value was improved in all the processed samples. The maximum and minimum average microhardness values were 128.2 and 98.99 Hv for samples DP9 and SP1. As per the Hall-Petch correlation, producing refined grains in SCs enhances their mechanical properties. The presence of fine grain improves the strength of the material. The observed increase in hardness in the SCs, likely due to the greater pinning effect of particles, is linked to the Orowan strengthening mechanism. This mechanism strengthens a material by creating obstacles, such as dislocations, that impede the movement of other dislocations. In the context of this study, it seems that the Orowan strengthening mechanism is contributing to the higher hardness of the SCs. Furthermore, a tunnel defect initially observed in the as-received (AS) sample completely vanished after the second pass. This disappearance suggests an improvement in material movement and a more uniform distribution of particles. This enhancement in material movement is attributed to the friction stir processing (FSP) or the similar process being described, which appears to have successfully reduced structural defects and improved the particle distribution within the material.

Tensile testing

To evaluate the UTS of developed SCs, test specimens with a gauge length of 30 mm were machined to a thickness of 3.5 mm for composites processed with

different shoulder diameters for a single pass and 21 mm shoulder diameter for a second pass FSP, respectively. The optimized outcomes of the investigation are displayed in Figure 12. These results represent the outcomes obtained following the optimization process that are the most advantageous or optimal.

Figure 12 depicts the maximum and minimum UTS found in SP₉ and SP₅ samples after a single pass and DP₉ and DP₁ after the second pass, respectively, which was lower than the UTS of the BM (300.9 MPa) after both passes and can be attributed to Fe–Al reinforced agglomeration. The UTS of sample SP₅ is 56.4 MPa, much less than BM, due to aggregation of Fe–Al reinforcement particles and tunnel defect. Aggregation and tunnel defects cause a reduction in the strength at the interfaces between the reinforcement particles and the BM, which can lead to crack propagation. Also, these clusters and tunnels take a small load and decrease the load-bearing capacity. However, after the second pass, the UTS of this sample increases to 229.8 MPa due to the elimination of tunnel defect and better particle distribution. Also, closely occupied dense reinforcement close to TMAZ (as depicting from Figures 4(b) and 5(b)) also reasons for poor bonding amongst the reinforced particles and the metal matrix. Thus, the mechanical properties of the fabricated composites are strictly correlated to the agglomeration of the reinforcement. Therefore, it is crucial to have a uniform particle distribution without any aggregation when fabricating SCs, as this is a fundamental requirement for their effective production. Also, after double-pass FSP refining the microstructure of samples. In the first pass, the rotating tool stirs and blends the material, resulting in a reduction in grain size and increased uniformity within the material. Smaller and more uniformly sized grains often lead to improved mechanical properties, including higher UTS. But after the second pass, the tool further refines the grains even

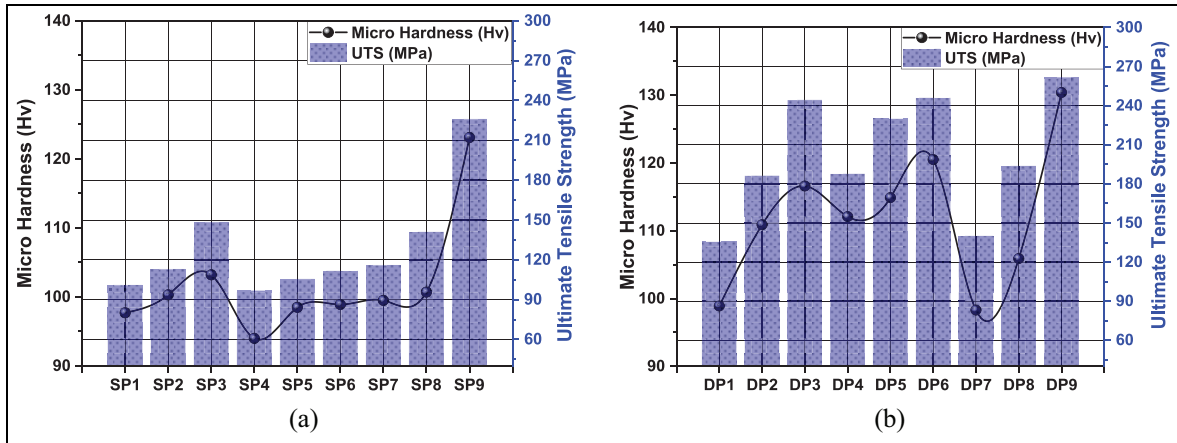


Figure 12. The ultimate tensile strength (UTS) and micro hardness of (a) single pass and (b) double-pass FSP specimens.

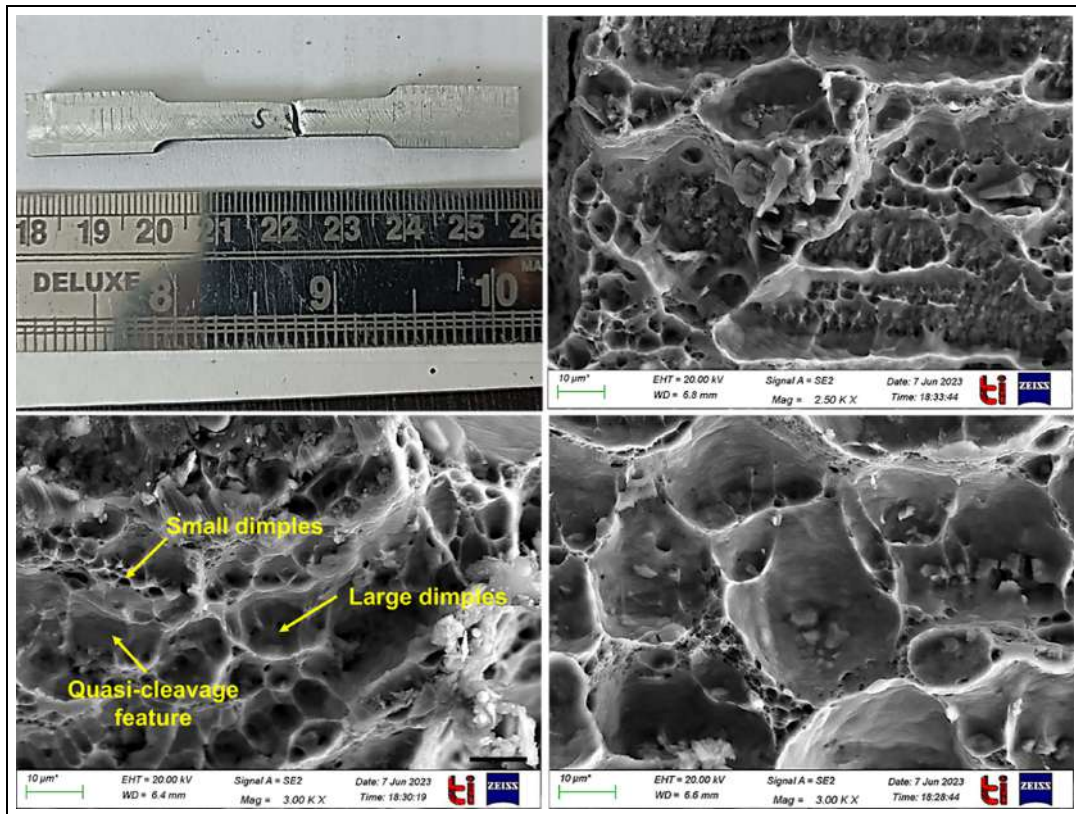


Figure 13. Represent the tensile fracture sample and FeSEM analysis of tensile fracture surface of DP9 FSP sample.

smaller and more uniform, which results boost UTS of double pass samples. Another factor contributing to the potential enhancement of UTS during double-pass FSP is the introduction of alloying effects. In the first pass, material from the surrounding regions is mixed with the base material being processed, potentially causing changes in the material's composition. This alloying can modify the material's characteristics, possibly improving its UTS. The second pass then confirms the even distribution of reinforcement within the samples.

SEM analysis of fracture sample

Figure 13 illustrates the FE-SEM analysis of fracture surface of the DP9 sample. In Figure 13, the morphology exhibits numerous larger dimples and voids, indicating a typical ductile fracture behaviour. Smaller holes are distributed around the larger dimples due to grain refinement resulting from the FSP process. The fracture surface of the AMCs displays neither the typical characteristics of ductile nor brittle fractures, suggesting a mixed mode of ductile-brittle failure.

As depicted in Figure 13, the dimples on the fracture surface of AMCs are noticeably smaller, and localized small planes resembling quasi-cleavage fracture features are present. During tensile loading, the reinforcement hinders dislocation slip, creating stress concentration points that lead to void nucleation around the reinforcement. Subsequently, the voids coalesce and grow with increased loading, resulting in failure. Grain boundaries and triple junctions also facilitate crack nucleation in the AMCs. The Fe act as pinning points, improving the strength by altering the crack propagation direction and retarding fracture occurrence. Simultaneously, the pull-out of Fe particles, along with their interruption effect on dislocation slip, contributes to the increased strength of the AMCs.

Conclusion

This study used single-pass and double pass FSP procedures to produce in situ AA 5083-H111/Al-Fe surface composites. The results of the investigation are as follows:

- During the double pass FSP, the disintegration of Fe-Al reinforced particle and metal matrix grains occurs under the combined effect of plastic strains and stirring action of the FSP tool.
- Miniature tunnel defects were present in samples processed at 710 and 1120 rpm. No tunnel defects are observed in samples when processed at 900 rpm.
- In the single pass run, reinforced particles were not spread efficiently in the matrix and formed clusters in the SZ of SCs. However, alteration in tool travel direction (ATD) improves powder particle distribution after a second pass. For complete homogenization of reinforcement, several FSP passes are required.
- During the process of FSP, the formation of intermetallic Al_3Fe_4 was confirmed by XRD analysis.
- The tensile test shows that the UTS of SCs was less than the BM. This was mainly ascribed to particle aggregation. A maximum UTS of 253.6 MPa was found in the sample after the second pass FSP.
- Maximum microhardness of about 128.2 Hv was achieved after the second pass FSP.
- The FeSEM analysis of the fractured surface of the FSP composite sample indicates that ductile and quasi-cleavage fractures characterize the failure mode.



Declaration of conflicting interests

The author(s) declared no potential conflicts of interest with respect to the research, authorship, and/or publication of this article.

Funding

The author(s) received no financial support for the research, authorship, and/or publication of this article.

ORCID iDs

Varun Singhal  <https://orcid.org/0000-0001-9075-9210>
Vivek Kumar Jain  <https://orcid.org/0000-0001-5666-4322>

References

1. Miracle DB. Metal matrix composites – from science to technological significance. *Compos Sci Technol* 2005; 65(15–16): 2526–2540.
2. Sharma M, Singhal V, Gupta A, et al. Microstructural, mechanical and wear characteristics of industrial waste (brass slag) reinforced LM30 alloy-based composite. *Silicon [Internet]*. Epub ahead of print 14 September 2023. DOI: 10.1007/s12633-023-02665-3.
3. Singhal V, Gupta A, Pandey OP, et al. Investigate the optical and dry sliding wear behavior of solid lubricated sillimanite reinforced aluminum metal matrix composite. *Mater Today Proc [Internet]*. Epub ahead of print 2 March 2023. DOI: 10.1016/j.matpr.2023.02.196.
4. Hashim J, Looney L and Hashmi MSJ. Metal matrix composites: production by the stir casting method. *Mater Today Proc* 2017; 4(2): 3458–3465.
5. Abdizadeh H, Ebrahimifard R and Baghchesara MA. Investigation of microstructure and mechanical properties of nano MgO reinforced Al composites manufactured by stir casting and powder metallurgy methods: a comparative study. *Compos Part B Eng [Internet]* 2014; 56: 217–221.
6. Banhart J. Manufacture, characterisation and application of cellular metals and metal foams. *Prog Mater Sci* 2001; 46(6): 559–632.
7. Ghosh SK and Saha P. Crack and wear behavior of SiC particulate reinforced aluminium based metal matrix composite fabricated by direct metal laser sintering process. *Mater Des [Internet]* 2011; 32(1): 139–145.
8. Xu J, Zou B, Tao S, et al. Fabrication and properties of $Al_2O_3-TiB_2-TiC/Al$ metal matrix composite coatings by atmospheric plasma spraying of SHS powders. *J Alloys Compd* 2016; 672: 251–259.
9. Scott VD. An introduction to metal matrix composites. *Compos Sci Technol* 1987; 51: 121–130.
10. Mishra RS and Mahoney MW. Friction stir welding and processing. *ASM Int* 2007; 368: 1–78.
11. Mishra RS and Ma ZY. Friction stir welding and processing. *Mater. Sci. Eng. R Rep* 2005; 50: 1–78.
12. Sharma V, Prakash U and Manoj Kumar BV. Tribological characteristics of friction stir processed graphite and tin/LM24 surface composites. *Friction* 2021; 9(3): 569–582.
13. Balakrishnan M, Dinaharan I, Palanivel R, et al. Effect of friction stir processing on microstructure and tensile behavior of AA6061/Al3Fe cast aluminum matrix composites. *J Alloys Compd* 2019; 785: 531–541.
14. Ke L, Huang C, Xing L, et al. Al – Ni intermetallic composites produced in situ by friction stir processing. *J Alloys Compd [Internet]* 2010; 503(2): 494–499.

15. Garg T, Mathur P, Singhal V, et al. Underwater friction stir welding: an overview. *Int Rev Appl Eng Res* 2014; 4(2): 2248–9967.
16. Azimi-Roeeen G, Kashani-Bozorg SF, Nosko M, et al. Reactive mechanism and mechanical properties of in-situ hybrid nano-composites fabricated from an Al-Fe₂O₃ system by friction stir processing. *Mater Charact* 2017; 127: 279–287.
17. Hsu CJ, Chang CY, Kao PW, et al. Al – Al₃Ti nano-composites produced in situ by friction stir processing. *Acta Mater* 2006; 54(70): 5241–5249.
18. Gangil N, Siddiquee AN and Maheshwari S. Aluminium based in-situ composite fabrication through friction stir processing: a review. *J Alloys Compd* 2017; 715: 91–104.
19. Nelson TW, Steel RJ and Arbogast WJ. In situ thermal studies and post-weld mechanical properties of friction stir welds in age hardenable aluminium alloys. *Sci Technol Weld Join* 2003; 8(4): 283–288.
20. Thomas WM, Nicholas ED, Needham JC, et al. Improvements to friction welding. International Patent Application PCT/GB92/02203 and GB Patent Application No.9125978.8., UK Patent Office, London, 1991.
21. Ezuber H, El-Houd A and El-Shawesh F. A study on the corrosion behavior of aluminum alloys in seawater. *Mater Des* 2008; 29(4): 801–815.
22. Kurt HI. Influence of hybrid ratio and friction stir processing parameters on ultimate tensile strength of 5083 aluminum matrix hybrid composites. *Compos Part B Eng [Internet]* 2016; 93: 26–34.
23. Zhang Q, Xiao BL, Wang D, et al. Formation mechanism of in situ Al₃Ti in Al matrix during hot pressing and subsequent friction stir processing. *Mater Chem Phys* 2011; 130: 1109–1117.
24. Hsu CJ, Kao PW and Ho NJ. Ultrafine-grained Al – Al₂Cu composite produced in situ by friction stir processing. *Ser Mater* 2005; 53: 341–345.
25. Qian J, Li J, Xiong J, et al. In situ synthesizing Al₃Ni for fabrication of intermetallic-reinforced aluminum alloy composites by friction stir processing. *Mater Sci Eng A [Internet]* 2012; 550: 279–285.
26. Shahi A, Sohi MH, Ahmadkhaniha D, et al. In situ formation of Al–Al₃Ni composites on commercially pure aluminium by friction stir processing. *Int J Adv Manuf Technol* 2014; 75(9–12): 1331–1337.
27. Lee IS, Kao PW, Chang CP, et al. Formation of Al-Mo intermetallic particle-strengthened aluminum alloys by friction stir processing. *Intermetallics* 2013; 35: 1–6.
28. Lee IS, Kao PW and Ho NJ. Microstructure and mechanical properties of Al – Fe in situ nanocomposite produced by friction stir processing. *Intermetallics* 2008; 16: 1104–1108.
29. Anvari SR, Karimzadeh F and Enayati MH. Wear characteristics of Al-Cr-O surface nano-composite layer fabricated on Al6061 plate by friction stir processing. *Wear [Internet]* 2013; 304(1–2): 144–151.
30. Azizieh M, Mazaheri M, Balak Z, et al. Fabrication of Mg/Al₁₂Mg₁₇ in-situ surface nanocomposite via friction stir processing. *Mater Sci Eng A* 2018; 712: 655–662.
31. Niyomwas S. Preparation of aluminum reinforced with TiB₂-Al₂O₃-Fe x Al y composites derived from natural ilmenite. *Int J Self-Propagating High-Temperature Synth* 2010; 19(2): 150–156.
32. Sarkari Khorrami M, Samadi S, Janghorban Z, et al. In-situ aluminum matrix composite produced by friction stir processing using FE particles. *Mater Sci Eng A* 2015; 641: 380–390.
33. Azizieh M, Pourmodheji R, Larki AN, et al. Effect of multi-pass friction stir processing on the microstructure and hardness of AA1100/Al₁₃Fe₄ in situ composites. *Mater Res Express* 2019; 6: 046558.
34. Dinaharan I and Murugan N. Optimization of friction stir welding process to maximize tensile strength of AA6061/ZrB₂ in-situ composite butt joints. *Met Mater Int* 2012; 18(1): 135–142.
35. Gopalakrishnan S and Murugan N. Production and wear characterisation of AA 6061 matrix titanium carbide particulate reinforced composite by enhanced stir casting method. *Compos Part B Eng* 2012; 43(2): 302–308.
36. Murugan N and Ashok Kumar B. Prediction of tensile strength of friction stir welded stir cast AA6061-T6/AlNp composite. *Mater Des [Internet]* 2013; 51: 998–1007.
37. Seighalani KR, Givi MKB, Nasiri AM, et al. Investigations on the effects of the tool material, geometry, and tilt angle on friction stir welding of pure titanium. *J Mater Eng Perform* 2010; 19(7): 955–962.
38. Rathee S, Maheshwari S, Siddiquee AN, et al. Investigating effects of groove dimensions on microstructure and mechanical properties of AA6063/SiC surface composites produced by friction stir processing. *Trans Indian Inst Met* 2017; 70(3): 809–816.
39. Gangil N, Maheshwari S and Siddiquee AN. Influence of tool pin and shoulder geometries on microstructure of friction stir processed AA6063/SiC composites. *Mech Ind* 2018; 19(2): 211.
40. Dolatkhah A, Golbabaee P, Besharati Givi MK, et al. Investigating effects of process parameters on microstructural and mechanical properties of Al₅₀₅₂/SiC metal matrix composite fabricated via friction stir processing. *Mater Des* 2012; 37: 458–464.
41. Gan YX, Solomon D and Reinbolt M. Friction stir processing of particle reinforced composite materials. *Materials (Basel)* 2010; 3(1): 329–350.
42. Khalid A Al-Ghamdi, Hussain G and Hashemi R. *Fabrication of metal-matrix AL7075T651/TiN nano composite employing friction stir process*. *Proc Inst Mech Eng Part B J Eng Manuf* 2015; 231: 1319–1331.
43. Shojaeefard MH and Akbari M. Effect of tool pin profile on distribution of reinforcement particles during friction stir processing of B 4 C/aluminum composites. *Proc Inst Mech Eng Pt L J Mater Des Appl* 2018; 232(8): 637–651.
44. Li Y, Murr LE and McClure JC. Flow visualization and residual microstructures associated with the friction-stir welding of 2024 aluminum to 6061 aluminum. *Mater Sci Eng A Mat Sci Eng A-Struct* 1999; 271: 213–223.
45. Reynolds AP. Visualisation of material flow in autogenous friction stir welds. *Sci Technol Weld Join* 2000; 5(2): 120–124.
46. Jiang WH and Kovacevic R. Feasibility study of friction stir welding of 6061-T6 aluminium alloy with AISI 1018 steel. *Proc Instn Mech Engrs Part B J Eng Manuf* 2004; 218: 1323–1332.

Appendix*Notation*

ACW	Anti clockwise	RRVMC	Retrofitted robust verticals milling machine
AS	Advancing side	RS	Retreating side
AMC	Aluminium metal matrix composite	RZ	Reinforced zone
BM	Base alloy	SC	Surface composite
CTTD	Change in tool travel direction	SPD	Severe plastic deformation
FSP	Friction stir process	SZ	Stir zone
MMC	Metal matrix composite	TMAZ	Thermomechanical affected zone
		TRS	Tool rotation speed
		TSD	Tool shoulder diameter